Scientific Reports

https://doi.org/10.1038/s41598-025-32997-6

Article in Press

# Femtogram-level VEGF detection via PEG-directed gold nanostructured electrochemical immunosensor

Received: 2 August 2025

Accepted: 15 December 2025

Published online: 20 December 2025

Cite this article as: Mirmohamadi B., Moshaii A., Yarjoo S. *et al.* Femtogram-level VEGF detection via PEG-directed gold nanostructured electrochemical immunosensor. *Sci Rep* (2025). https://doi.org/10.1038/s41598-025-32997-6

**Badrossadat Mirmohamadi, Ahmad Moshaii, Sadaf Yarjoo, Hossein Siampour, Salim al-Hafyan & Reza H. Sajedi**

# Femtogram-Level VEGF Detection via PEG-Directed Gold Nanostructured Electrochemical Immunosensor

Badrossadat Mirmohamadi[1], Ahmad Moshaii[1,2]*, Sadaf Yarjoo[1], Hossein Siampour[1], Salim al-Hafyan[3], Reza. H. Sajedi[3]

[1]Department of Physics, Tarbiat Modares University, Tehran, P.O. Box 14115-175, Iran
[2]Department of Sensor and Biosensor, Faculty of Interdisciplinary Sciences and Technologies, Tarbiat Modares University, Tehran, P.O. Box 14115-336, Tehran, Iran
[3]Department of Biochemistry, Faculty of Biological Sciences, Tarbiat Modares University, Tehran, P.O. Box14115-154, Iran

*Email: moshaii@modares.ac.ir



## Abstract

This study presents a novel electrochemical immunosensor designed for the highly sensitive detection of vascular endothelial growth factor (VEGF). The sensor utilizes gold nanostructures grown on fluorine-doped tin oxide (FTO) electrodes through a polyethylene glycol (PEG)-mediated electrochemical process. Fabrication involves a two-step immobilization strategy, combining physical vapor deposition (PVD) of a gold thin film with thermal annealing. The nanostructured electrode is subsequently modified electrochemically via PEG mediation, followed by antibody functionalization to enhance binding specificity. PEG-mediated control over nanostructure growth yields irregular short nanorods and leaf-like dendrites, significantly enhancing sensor performance. Extensive electrochemical analyses, including cyclic voltammetry and impedance spectroscopy, confirm improved sensitivity and stability. The optimized immunosensor achieves an ultralow detection limit of 6fg/mL (corresponding to ~9500 VEGF molecules in 60 µL, and a broad linear detection range of 10 fg/mL to $10^5$ fg/mL, with excellent reproducibility. Given VEGF's pivotal role in angiogenesis and tumor progression, this ultrasensitive platform offers a promising tool for early cancer diagnostics.

**Keywords:** Electrochemical Immunosensor, PEG-Mediated Gold Nanostructures, Vascular Endothelial Growth Factor (VEGF), Early Cancer Detection, Nanomaterial-based Biosensor

## 1.Introduction

Biosensors represent a major advancement in analytical science, selectively interacting with specific analytes and translating these interactions into measurable signals that can be interpreted by readout systems[1]. Immunosensors, a key subset of biosensors, utilize the highly specific binding between antigens and antibodies to detect a wide range of biomolecules[1][2]. Due to their high specificity and sensitivity, these sensors play a critical role in medical diagnostics[3][4][5][6][7], environmental monitoring[8], and food safety[9]. Immunosensors enable rapid and accurate identification of disease markers[6][7][8][10], pathogens[11], and contaminants[8][10], establishing them as indispensable tools in both clinical and research applications.

A notable type of immunosensors is one specifically designed to detect vascular endothelial growth factor (VEGF). VEGF plays a crucial role in angiogenesis, the process of forming new blood vessels, which is essential for tumour growth and metastasis[12][13][14][15]. Consequently, the development of sensitive and reliable immunosensors for detecting VEGF holds significant promise for early cancer diagnosis and prognosis, underscoring the need for continued research in this field[2].

Various techniques, including physical vapor deposition (PVD), chemical vapor deposition (CVD), hydrothermal synthesis, and synthesis using reducing agents, have been widely utilized to deposit gold nanostructures onto electrode surfaces[16][17][18][13][19][20]. These methods have effectively improved the sensing capabilities of the electrodes, offering advantages such as higher electron transfer rates, enhanced electrocatalytic activity, and improved biorecognition performance. In addition, signal amplification strategies, such as redox cycling [21][22][23] are frequently employed to achieve femtogram-level sensitivity.

Recent advancements in electrochemical VEGF immunosensors have utilized the unique physicochemical properties of nanomaterials to enhance sensor performance. Incorporating nanostructures into these immunosensors has been shown to substantially increase the active surface area, charge transfer efficiency, and overall sensor sensitivity[24][25]. Various nanomaterials are employed in electrode surface development, with gold nanostructures being

particularly favoured for their excellent conductivity, compatibility with biological systems, and resistance to rapid oxidation[13][26][27]. For instance, Yarjoo et al. reported gold nanostructure-enhanced VEGF detection with a limit of detection (LOD) of 0.5 pg/mL [28], while Rezaei et al. (2024) achieved label-free detection using phage-displayed VHH on glassy carbon electrodes, though without nanostructure optimization (LOD: ~1 pg/mL) [29].

The primary objective of this study is to develop a novel gold nanostructured electrode for the ultrasensitive electrochemical detection of VEGF. The sensor incorporates gold nanostructures deposited onto fluorine-doped tin oxide (FTO) electrodes through a two-step surface modification process [30][31][32]. First, a gold thin film is physically deposited onto the FTO substrate, followed by an annealing procedure to enhance the surface. Subsequently, the gold nanostructures are electrochemically modified using polyethylene glycol (PEG) as a surfactant. The incorporation of PEG significantly improves the sensing properties of the electrochemical immunosensor by directing the controlled growth of gold nanostructures, resulting in time-dependent morphologies, including small leaf-like dendrites at longer deposition times.

Here, we employ a camelid single-domain antibody (VHH, nanobody) directed against the receptor-binding domain of VEGF, a strategy that has recently been demonstrated for highly sensitive and specific detection of biomarkers in electrochemical immunosensors[33][34][35][36]. A detailed protocol for antibody immobilization on the gold nanostructures enables efficient detection of VEGF. Electrochemical analyses, including cyclic voltammetry (CV) and electrochemical impedance spectroscopy (EIS), confirm the electrode’s enhanced sensitivity and stability. The optimized sensor achieved a detection limit as low as 6 fg/mL for VEGF, with excellent reproducibility, establishing it as a highly reliable tool for precise measurements.

The selective PEG adsorption and applied potential in this work direct a morphological transition that yields anisotropic gold nanostructures not previously demonstrated in VEGF biosensing. When integrated with VHH nanobodies, these tailored architectures enable the ultralow detection limit of 6 fg/mL, representing a notable advancement over our earlier platform [28]. In contrast to that study, which utilized PVD-annealed and chemically dealloyed nanoporous gold electrodes, the present work employs a PEG-mediated electrochemical deposition approach that provides enhanced control over gold nucleation and growth. This method produces a broader spectrum of nanoscale morphologies, including nanoporous clusters, short

nanorods, and branched dendrites, that cannot be obtained through the conventional PVD/annealing/dealloying pathway.

## 2. Experimental section

### 2.1. Materials and instruments

Polyethylene glycol (PEG) has been employed to control the growth of nanoparticles, ensuring their size is appropriately scaled to the nanoscale. PEG's molecular formula is $C_{2n}H_{4n+2}O_{n+1}$, where n denotes the average number of ethylene oxide units. The molar mass of PEG is given by 44.05n+18.02 g/mol, and the average density of PEG is often cited as approximately 1.125 g/cm$^3$.The electrolyte solution for electrochemical coating consisted of sulfuric acid $H_2SO_4$, gold salt ($HAuCl_4$, and polyethylene glycol 600 (PEG 600). A three-electrode system was employed for the electrochemical deposition, consisting of a working electrode, a counter electrode, and a reference electrode. The potential is measured between the reference electrode and the working electrode, while the current is measured between the working and counter electrodes.

The buffer solution used in the experiments was phosphate-buffered saline (PBS) with a pH of 7.4.Other chemicals included mercaptoacetic acid (MAA) with a purity exceeding 99%, 1-Ethyl-3-(3dimethylaminopropyl) carbodiimide (EDC), and N-Hydroxysuccinimide (NHS), both with a purity of 99%, acetone with a purity greater than 99.5%, potassium ferricyanide ($K_3Fe(CN)_6$), potassium ferrocyanide ($K_4Fe(CN)_6$), and potassium chloride (KCl), all with purities 99%, as well as glucose with a purity of 99.5%, were procured from Sigma-Aldrich and are of analytical grade.

Additional reagents included gelatine, variable heavy-chain antibody (VHH) against VEGF antigens, ethanol (99.9% purity), and potential interferents used for selectivity testing: interleukin-1β (IL-1β), insulin-like growth factor-1 (IGF-1), and interleukin-2 (IL-2). All reagents were of analytical grade and purchased from Sigma-Aldrich. Ultrapure water with a resistivity of 18.2 MΩ.cm was used in the preparation of all solutions. The fabricated electrodes were characterized using field emission scanning electron microscopy (FE-SEM) equipped with energy-dispersive X-ray spectroscopy (EDS) (FEI Nova NanoSEM-450).

### 2.2. Fabrication of the Immunosensor

The fabrication of the VEGF electrochemical immunosensor involved a two-phase electrode modification strategy designed to maximize sensitivity and

specificity for ultrasensitive detection of VEGF in biological samples, illustrated in Fig. 1. The steps are detailed as follows:

**Phase 1, Formation of Gold Seeds:** The fabrication started with the preparation of a clean FTO substrate, which was ultrasonically cleaned in acetone, ethanol, and deionized water. A 5nm thin layer of gold was deposited on the FTO surface via thermal evaporation in a high-vacuum PVD chamber ($10^{-6}$ Torr) using gold of 99.99% purity[32][37][38][39] This initial gold layer served as the seed layer, critical for subsequent nanostructure development. After deposition, the FTO substrate was annealed at 500°Cfor 20 hours to facilitate the formation of stable Au seed nanoparticles. This annealing process allowed for controlled reorganization of the gold atoms[40], establishing a conductive, textured base layer ideal for enhancing electron transfer rates and sensor stability in later stages[26][40].

**Phase 2, Electrochemical Growth of Gold Nanostructures:** Following seed formation, the annealed Au-coated FTO electrode was immersed in an electrolyte solution containing sulfuric acid, $HAuCl_4$, and PEG to support the growth of Au nanostructures. Electrochemical deposition was carried out in this solution, where controlled potential conditions promoted the development of a porous, rough gold surface. This nanostructured morphology significantly increased the effective surface area of the electrode, improving both binding capacity and signal sensitivity of the immunosensor.

With the electrode structure optimized, surface biofunctionalization was initiated. Linkers such as mercaptoacetic acid (MAA), EDC, and NHS were sequentially applied to facilitate stable antibody attachment, similar to those reported in the literature [42][43]. The receptor binding domain of VEGF ($VEGF_{8\text{-}109}$) as an antigen and the surface-displayed single-domain antibody (VHH) against VEGF in Escherichia coli were previously provided by Rezaei et al. [44].

The pellet fraction of the cell lysate from VHH-displaying E. coli was immobilized on the functionalized electrode surface. VHH antibodies, also known as nanobodies, are single-domain fragments (~15 kDa) derived from camelid heavy-chain antibodies. Their small size, high thermal and chemical stability, and strong refolding capacity enable dense and oriented immobilization on nanostructured gold surfaces, minimizing steric hindrance and enhancing antigen accessibility, advantages that make them particularly suitable for electrochemical biosensing applications. To ensure selectivity, non-specific binding sites were blocked using gelatin. This step ensured

selective binding of VEGF to the antibody-functionalized regions of the electrode. Gelatin was chosen because it forms a dense and uniform monolayer on gold surfaces (~3.3 ng/mm²) [45] effectively minimizing non-specific adsorption and maintaining film stability during electrochemical measurements.

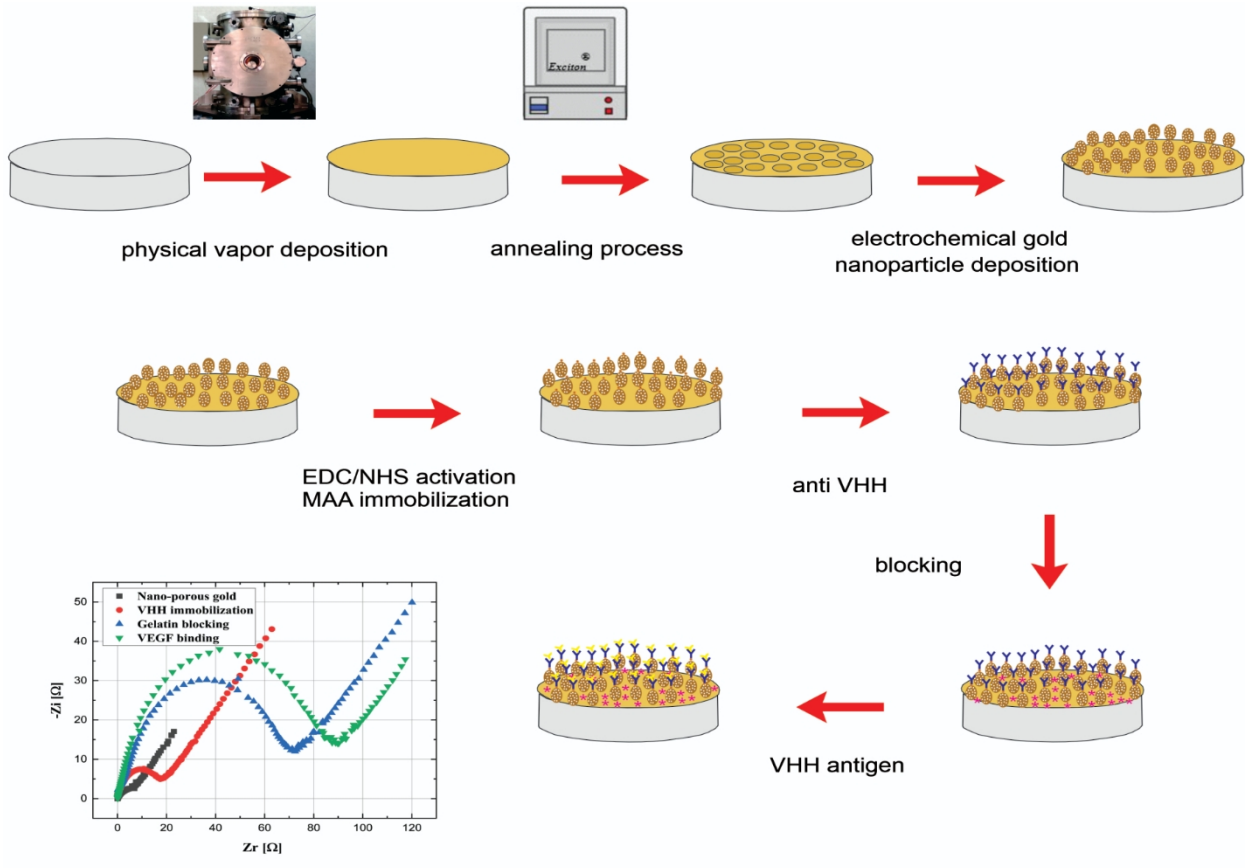


**Figure 1.** Schematic illustration of the fabrication steps for the VEGF electrochemical immunosensor on a nanoporous gold electrode. The process includes (i) deposition of a gold seed layer onto an FTO substrate by PVD and subsequent annealing, (ii) electrochemical deposition using PEG to generate nanoporous gold, and (iii) biofunctionalization through MAA attachment, EDC/NHS activation, VHH immobilization, and gelatine blocking to enable selective VEGF recognition.

## 2.3 Electrochemical Measurements

Cyclic voltammetry and electrochemical impedance spectroscopy were carried out using an Origalys Potentiostat / Galvanostat system in a conventional three-electrode configuration. The modified FTO electrode served as the working electrode, a gold auxiliary plate as the counter electrode, and an Ag/AgCl electrode as the reference. The CV measurements

were performed in 0.1 M PBS, (pH 7.4) containing 5 mM $[Fe(CN)_6]^{3-/4-}$ and 0.1 M KCl as the supporting electrolyte. Scans were recorded within a potential window of –0.2 to +0.6 V at scan rates ranging from 10 to 100 mV $s^{-1}$. EIS measurements were conducted in the same electrolyte over a frequency range of 0.1 Hz to 100 kHz, with an AC amplitude of 5 mV at the open-circuit potential. All measurements were performed at room temperature (~25 °C).

## 3. Results and Discussions

### 3.1. Morphological Characterization of Nano-Porous Gold Electrodes

Figure 2 illustrates the effect of varying electrochemical potentials and deposition times on the morphological properties of nanoporous gold electrodes, offering valuable insights into optimizing their structure for biosensing applications. The samples were prepared at two deposition potentials, 0 mV and 100 mV, and three deposition times: 5, 15, and 45 minutes.

At the deposition potential of V=0 mV, the growth process primarily promotes the development of a uniform porous structure, which becomes increasingly defined with longer deposition times. At t=5 min (Fig. 2a), the surface exhibits a sparse distribution of nanoscale gold clusters with relatively low density. By t=15 min (Fig. 2c), the clusters increase in size, appearing more interconnected and forming a more defined porous network. At t=45 (Fig. 2e), the surface morphology evolves into a highly interconnected porous structure with densely packed nanoscale features, with the extended deposition time enhancing the network's uniformity and coverage.

In contrast, at V=100 mV, the higher electrochemical potential significantly accelerates the deposition process and promotes the formation of dendritic structures due to enhanced nucleation and growth rates. At t=5 min (Fig. 2b), the morphology shows a higher density of gold clusters compared to V=0 mV, suggesting that the elevated potential increases the deposition rate. These clusters are larger and more uniform. By t=15 min (Fig. 2d), a distinct morphological transformation occurs, with the gold forming elongated, branched structures indicative of dendritic growth. At t=45 min (Fig. 2f), the dendritic structures are fully developed, covering the surface with intricate, tree-like formations.

The selection of deposition potentials of 0 and 100 mV is based on the distinct growth regimes they produce. At 0 mV, slow Au(I) reduction maintains a uniform ionic environment, producing densely packed nanoporous clusters.

At 100 mV, faster reduction generates steep concentration gradients that, together with PEG's facet-selective adsorption, drive anisotropic growth from isotropic nuclei to short nanorods (~15 min) and ultimately dendritic structures (~45 min). This potential-controlled morphological evolution differs mechanistically from dealloying in our previous work [28] and represents a key innovation of this study.

Notably, the structural evolution of the gold nanostructures follows a time-dependent pattern: irregular short nanorods emerge after 15 minutes of electrodeposition, while small leaf-like dendrites form after 45 minutes. This well-defined nanostructure enhances the electrode's electrochemical performance by improving charge transfer efficiency and increasing the availability of binding sites for antibody immobilization, ultimately leading to superior sensitivity and stability in VEGF detection.

The formation of dendritic nanostructures at higher applied potentials (–100 mV) and longer deposition times (45 min) arises from a transition in the gold growth mechanism [46][47]. At short times and lower potentials, isolated nucleation produces small, uniformly distributed gold clusters. As deposition proceeds, the accelerated reduction of Au(I) species exceeds ionic mass transport, creating concentration gradients and mass transfer limitations. This shift leads to diffusion-limited aggregation, favouring anisotropic, branched dendritic growth over the uniform growth. The presence of PEG further modulates this pathway by coordinating with gold ions and nascent clusters, stabilizing their surfaces and directing anisotropic extension through selective facet passivation. Consequently, PEG suppresses random isotropic deposition and promotes well-defined dendritic architectures with enhanced roughness and electroactive surface area, thereby improving biosensing performance.

The results in Fig.2 confirm that controlling electrochemical potential and deposition time is essential for tailoring the nano-porous gold electrode's surface morphology. The optimized electrode, with its high surface area and interconnected structure, provides a robust and efficient platform for sensitive and selective VEGF detection.

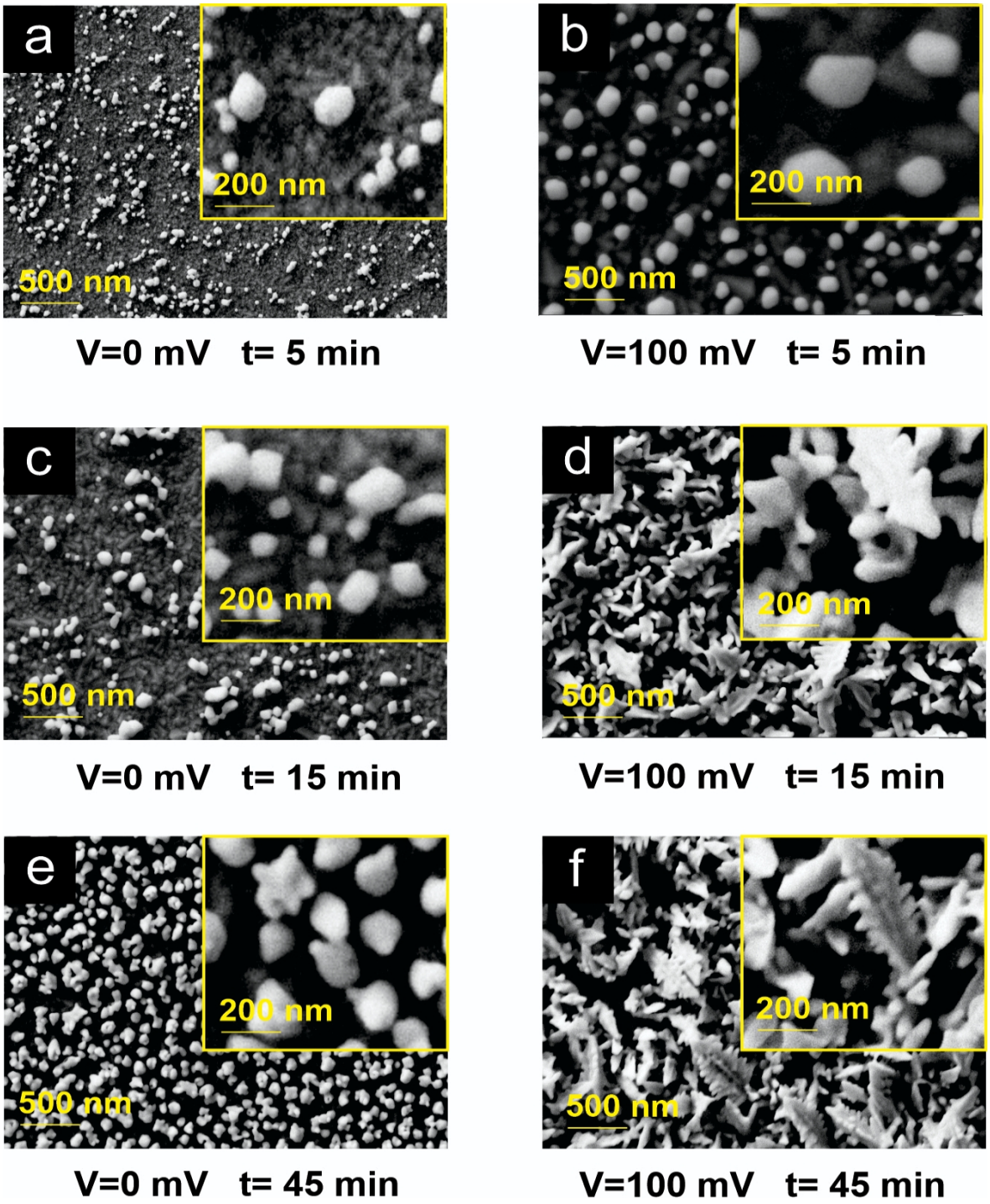


**Figure 2.** SEM images showing the effect of electrochemical potential (0 mV and 100 mV) and deposition time (5, 15, and 45 min) on the morphology of nanoporous gold electrodes: (a, c, e) 0 mV; (b, d, f) 100 mV.

In addition to FE-SEM imaging, energy-dispersive X-ray spectroscopy (EDS) analysis was performed on the optimized electrode prepared at –100 mV for 45 min to further confirm the elemental composition of the PEG-mediated

gold nanostructures. The EDS spectrum (Supplementary Information, Fig. S1) displays characteristic peaks corresponding to Au, along with discernible C and O signals originating from PEG molecules adsorbed on the nanostructured surface. The quantitative EDS results confirm the presence of approximately 7 wt% carbon and 8 wt% oxygen alongside gold, verifying the incorporation of PEG during the electrochemical growth process. These findings, consistent with the enhanced electrochemical response observed, provide additional evidence for successful PEG mediation and its role in directing nanostructure formation and charge transfer enhancement.

### 3.2. Electrochemical Characterization

The fabricated immunosensor was electrochemically characterized through CV and EIS, demonstrating reduced impedance and enhanced electron transfer, indicative of a high-sensitivity platform. Testing the sensor across a range of VEGF concentrations produced a linear calibration curve, confirming the sensor's ability to detect VEGF with a very low detection limit of 6 fg/mL.



Figure 3 illustrates the electrochemical analyses conducted to evaluate the enhancement in sensitivity provided by the modified gold electrode. The characterization process included CV and EIS for the performance comparison across different electrode modifications: a bare FTO electrode, the gold thin-film electrode, the annealed gold thin-film electrode (featuring nano-structuring), and the electrochemically modified (nano-porous) gold electrode. The CV results show a stepwise increase in current density across these configurations, indicating progressively improved electron transfer rates with each modification. This increase reflects the impact of nano-structuring and electrochemical porosity on the electrode’s surface area and conductivity, which are critical for enhancing sensor sensitivity.

The EIS results further support this observation, with Nyquist plots showing decreased impedance in the nano-porous gold electrode compared to the other configurations. The smaller semicircle diameter of the nano-porous electrode in the Nyquist plot demonstrates reduced charge-transfer resistance, which confirms the enhanced conductivity and active surface area of the nano-porous structure. The fitted EIS parameters in Table S1 (in Supplementary Information) quantitatively confirm the progressive improvement in the electrode’s interfacial properties through the modification steps. The charge transfer resistance ($R_{ct}$) decreases markedly from 76 Ω for the bare FTO to 6.8 Ω for the PEG-mediated nanoporous Au

electrode, reflecting enhanced electron transfer efficiency. These results agree with the Nyquist plots in Figure 3b, demonstrating the superior electrochemical performance of the PEG-modified nanoporous Au electrode.

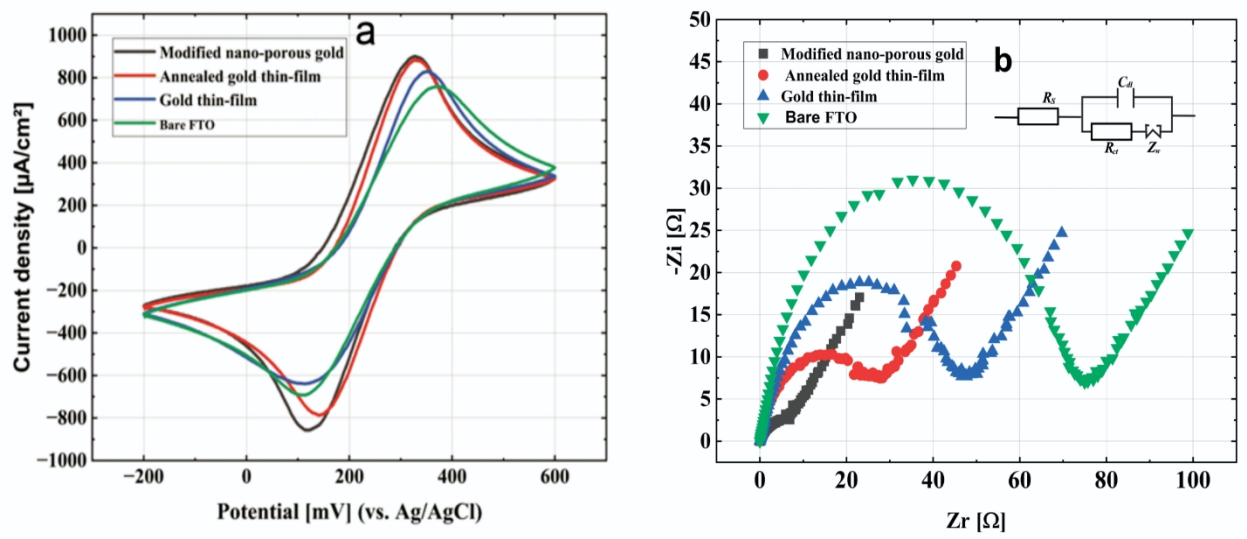


**Figure 3.** Electrochemical characterization of the modified electrodes: (a) Cyclic voltammetry (CV) and (b) electrochemical impedance spectroscopy (EIS) of four configurations—bare FTO, Au thin film, annealed Au thin film, and PEG-mediated nanoporous Au electrode—recorded in 5 mM $[Fe(CN)_6]^{3-/4-}$ containing 0.1 M KCl (scan rate: 50 mV/s). The corresponding equivalent circuit model used to fit the Nyquist plots is shown in the inset.

Figure 4 illustrates the electrochemical behaviour of the nano-porous gold electrode across different potential scan rates, providing insights into the diffusion-controlled electron transfer and reaction kinetics of the modified electrode. The figure includes CV curves for a range of scan rates and a plot of peak current versus the square root of the scan rate to assess the relationship between the scan rate and the current response.

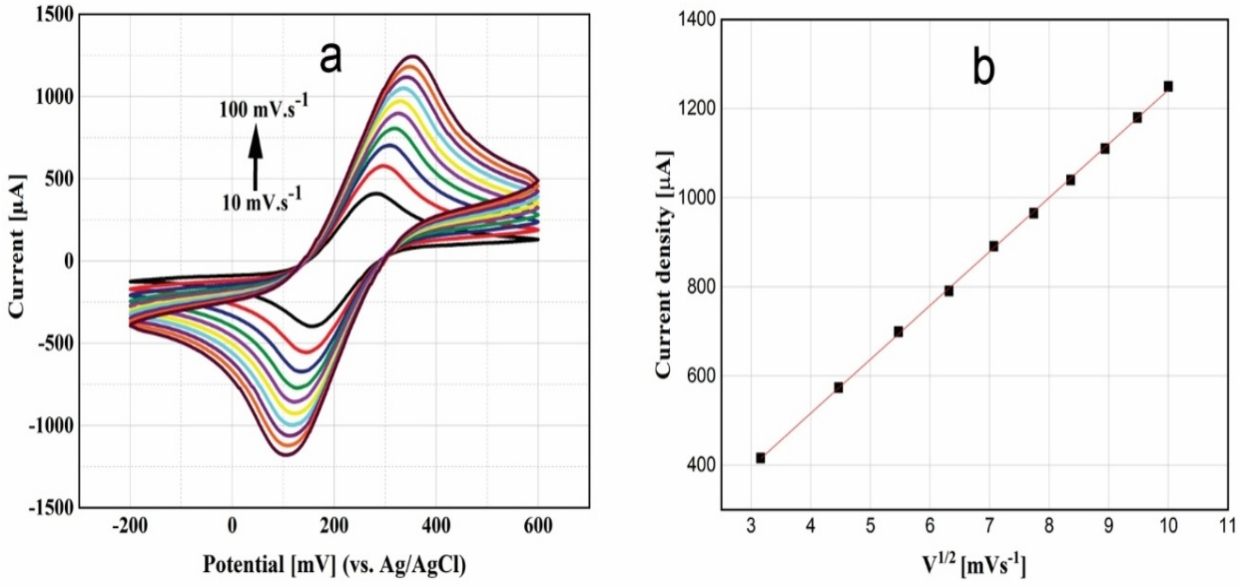


**Figure 4.**(a) CV curves of the nanoporous Au electrode recorded at scan rates from 10 to 100 mV/s in 0.1 M PBS (pH 7.4) containing 5 mM $[Fe(CN)_6]^{3-/4-}$ and 0.1 M KCl. (b) Corresponding plot of peak current versus the square root of the scan rate used for determination of diffusion-controlled behaviour.

In Fig. 4a, CV curves of the nano-porous gold electrode are shown for scan rates ranging from 10 to 100 mV/s. As the scan rate increases, a proportional rise in the anodic peak current is observed, indicating enhanced electron transfer at higher rates. This behaviour is characteristic of diffusion-controlled processes, where the rate of electron transfer is limited by the diffusion of analytes to the electrode surface. The increase in current with scan rate highlights the electrode's capacity to facilitate rapid electron transfer, a crucial feature for sensitive and responsive biosensing applications[48][49].

Figure 4b presents a linear plot of the anodic peak current as a function of the square root of the scan rate. The linearity of this plot confirms that the electron transfer process on the nano-porous gold electrode surface is diffusion-controlled. This linear relationship between current and the square root of scan rate is essential for biosensors, as it reflects efficient electron transfer kinetics and stability across various scan rates. This linearity also validates the electrode's effective porosity, which increases the surface area available for redox reactions and enhances overall electrochemical performance.

To quantitatively confirm the diffusion-controlled behaviour of the electrode, the Randles–Sevcik equation ($I_p = 2.69 \times 10^5\ n^{3/2}\ A\ D^{1/2}\ C_v^{1/2}$) was employed to analyse the CV data recorded at different scan rates. The peak current (*I*p)

increased linearly with the square root of the scan rate ($R^2$ = 0.998), indicating a diffusion-controlled electron transfer process. From the slope of this linear relationship (assuming n = 1, C = 2.5 mM, and D = 6.5 × $10^{-6}$ $cm^2/s$), the electroactive surface area of the PEG-modified nanoporous Au electrode was calculated to be approximately 1.99 $cm^2$.

To optimize the PEG concentration for directing gold nanostructure growth during electrochemical deposition, four PEG concentrations (0.56, 1.13, 1.63, and 2.63 g/L) were tested under constant synthesis conditions (100 mV, 45 min), and cyclic voltammetry was employed to determine the optimal concentration for electrode fabrication. The results, shown in Figure S2 (Supplementary Information), indicate that 1.13 g/L PEG yields the highest peak current density, reflecting optimal electron transfer efficiency and effective surface area compared to the other concentrations. Consequently, the electrode prepared with 1.13 g/L PEG was selected for subsequent experiments to maximize VEGF detection sensitivity, while other parameters (e.g., gold seed thickness, antibody concentration, incubation time, buffer) were maintained based on prior optimizations [28][46][50][51]to isolate and highlight the conceptual impact of PEG.

The PEG surfactant exerts a critical influence on the morphology and spatial distribution of gold nanostructures by functioning as a non-ionic surfactant and capping agent. During electrodeposition, PEG adsorbs onto both the electrode surface and the growing Au nuclei via van der Waals interactions and weak coordination with $Au^{3+}/Au^0$ species. This adsorption modifies the local interfacial energy and mass transport conditions, thereby suppressing uncontrolled coalescence and regulating nucleation density and growth anisotropy. In the presence of PEG, the morphology evolves from irregular short nanoparticles to dendritic, leaf-like architectures. This transition is attributed to surface passivation, which restricts adatom diffusion and promotes directional growth. Moreover, PEG-mediated deposition results in an increased electroactive surface area (from 1.73 $cm^2$ to 1.99 $cm^2$), thereby enhancing electron transfer kinetics and facilitating more efficient biomolecule immobilization on the sensor surface.

### 3.3. Immunosensing characterization

Figure 5 provides a detailed electrochemical analysis of the biofunctionalization process on the nano-porous gold electrode, highlighting each stage from the surface-displayed VHH immobilization to the final VEGF

antigen capture. The figure includes the CV curves and the EIS Nyquist plots that demonstrate the changes in electrochemical properties with each functionalization step.

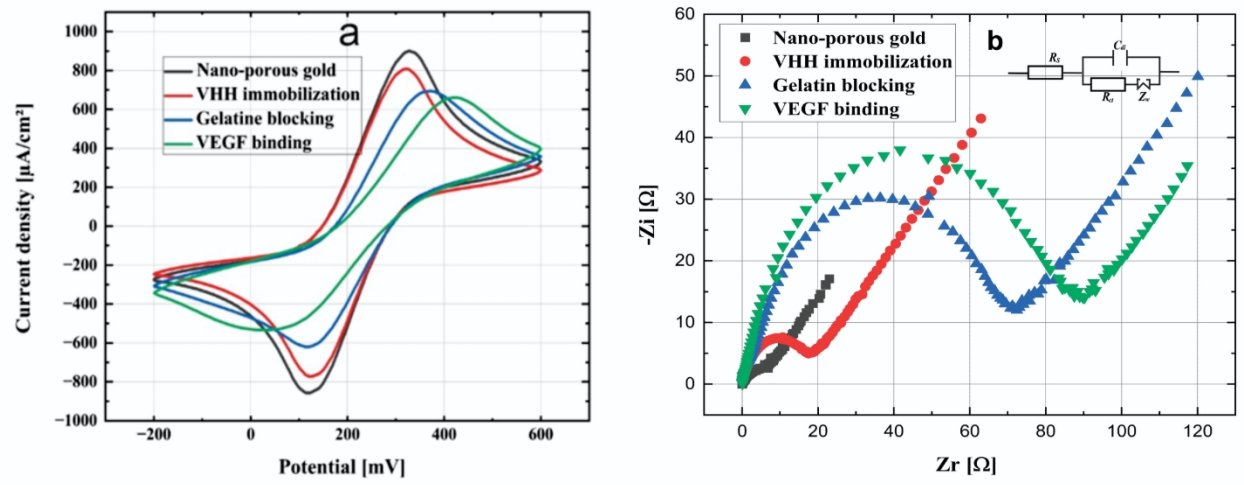


**Figure 5.** (a) CV curves and (b) Nyquist EIS plots recorded during successive modification steps of the nanoporous Au electrode: bare, VHH immobilized, gelatin-blocked, and VEGF-bound (1 pg/mL). Measurements were performed in 5 mM $[Fe(CN)_6]^{3-/4-}$ containing 0.1 M KCl at a scan rate of 50 mV/s.The corresponding equivalent circuit model used to fit the Nyquist plots is also shown in the inset.

Figure 5a displays CV curves conducted at the fixed scan rate of 50 mV/s for each major biofunctionalization stage including: (1) the initial nano-porous gold electrode, (2) after VHH antibody immobilization, (3) following gelatin blocking, and (4) after VEGF antigen binding. As functionalization progresses, a gradual decrease in peak current is observed, indicating increased surface resistance with each layer added. This current reduction is due to the insulating nature of the biomolecular layers, which hinders electron transfer at the electrode surface. The CV analysis confirms successful, stepwise assembly of bioactive components on the nano-porous electrode surface.

Figure 5b shows Nyquist plots obtained from the EIS measurements in a 2.5 mM $[Fe(CN)_6]^{3-/4-}$ solution, representing the same stages of electrode modification. The progression of Nyquist plots reveals an increasing semicircle diameter with each step, signifying a rise in charge transfer resistance as additional biomolecular layers are immobilized. This gradual impedance increase reflects the restricted electron transfer caused by the attachment of VHH antibodies, gelatin blocking, and finally the VEGF antigen binding. Each biofunctionalization step is clearly distinguished in the Nyquist plot, validating the successful assembly of the immunosensing layers. The

fitted EIS parameters in Table S2 (in Supplementary Information) further support the stepwise modification behaviour observed in Figure 5b. The charge transfer resistance increases progressively from 9 Ω for the bare electrode to 90 Ω after VEGF binding, confirming the successful sequential immobilization of VHH antibodies, gelatin blocking, and antigen attachment.

The progressive increases in charge transfer resistance and decreases in current response (from CV and EIS results) are consistent with successful antibody and antigen binding on the sensor surface. These findings demonstrate that the biofunctionalized nano-porous electrode is ready for ultrasensitive VEGF detection, with reliable layer-by-layer assembly ensuring specific antigen recognition and minimal nonspecific interactions.

Figure 6 illustrates the essential role of PEG in enhancing the sensitivity and quantitative performance of the VEGF immunosensor. The figure presents detailed EIS measurements and calibration curves to compare the sensor’s performance with and without PEG during electrode preparation.

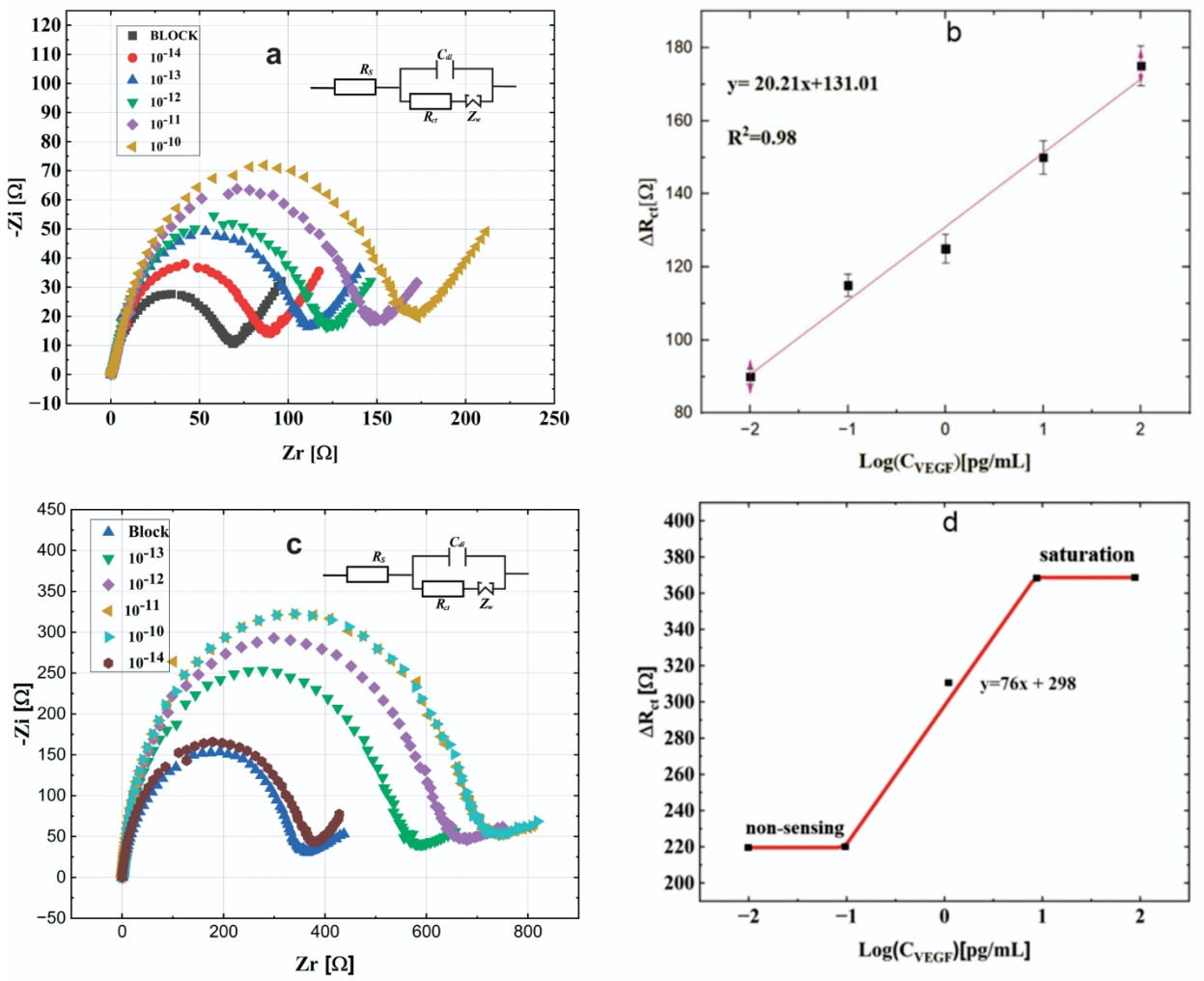


**Figure 6.** Comparison between PEG-modified and non-PEG-modified VEGF immunosensors:(a, c) Nyquist EIS plots recorded at different VEGF concentrations (10–$10^5$ fg/mL) in 5 mM $[Fe(CN)_6]^{3-}/^{4-}$/0.1 M KClwith the corresponding equivalent circuit model used to fit the Nyquist plots shown in the inset; (b, d) corresponding calibration curves derived from charge transfer resistance values.

The EIS Nyquist plots in Fig. 6a depict the sensor's response to a wide range of VEGF concentrations (10 to $10^5$fg/mL) for the PEG-modified nano-porous gold electrode. A systematic increase in the semicircle diameter is observed as the VEGF concentration rises, signifying an increase in charge transfer resistance. This increase reflects the progressive inhibition of electron transfer caused by surface-displayed VHH binding at the electrode surface. The correlation between $R_{ct}$ and VEGF concentration underscores the sensitivity and reliability of the sensor for quantifying VEGF through impedance-based analysis. The fitted EIS parameters in Table S3(in Supplementary Information) provide quantitative confirmation of the trends observed in Figure 6a. As the VEGF concentration increases from 10 fg/mL to $10^5$ fg/mL, the charge transfer resistance rises steadily from 71 Ω to 173

Ω, indicating increasing surface blockage due to antigen-antibody binding. This progressive rise in $R_{ct}$ corresponds to reduced electron transfer efficiency at the electrode-electrolyte interface. The results collectively verify the effective impedance-based detection of VEGF and highlight the high sensitivity of the PEG-modified nanoporous Au immunosensor.

The calibration curve for the PEG-mediated biosensor in Fig. 6b demonstrates a strong linear relationship across a broad dynamic range (10 to $10^5$fg/mL), with an exceptionally low detection limit (LOD) of 6fg/mL. The high linearity ($R^2$~0.98) emphasizes the biosensor's reproducibility and robustness, validating its applicability for ultrasensitive VEGF quantification. This wide detection range and ultra-low LOD highlight the sensor's utility in detecting trace levels of VEGF, which is crucial for early cancer diagnostics.

It should be noted that the LOD value of 6 fg/mL for the PEG-modified nanoporous gold electrode can be calculated using the following formula:

$$\mathrm{LOD} = 3.3\ {}^{\sigma}/_{S}$$

In this formula, σ represents the standard deviation of the blank response (or the lowest measured concentration), and S is the slope of the calibration plot[30][32] [33][34]. The LOD determination was based on n = 3 replicate measurements at the lowest VEGF concentration ($C_{min}$ = 10 fg $mL^{-1}$). The obtained standard deviation was σ = 8.5, and the calibration slope was calculated according to the semi-logarithmic relationship:

$$S=2.303\times \left(\frac{1}{C_{min}}\right)\times\left(\frac{d\ \Delta R_{ct}}{d\ \log C}\right)$$

where d(ΔRct)/d(logC)=20.21, as shown in Fig. 6b. Substituting these values into the equation yields an estimated LOD ≈ 6 fg $mL^{-1}$

It is valuable to estimate the number of VEGF molecules available for detection by the PEG-mediated biosensor at the lowest tested concentration (10 fg/mL, as shown in Fig. 6b). Given the 60 µL sample volume used in the experiment, the total mass of VEGF in the sample at this concentration is $6 \times 10^{-16}$ g. Using the molecular weight of VEGF (approximately 38,200 g/mol) and Avogadro's number ($6.02 \times 10^{23}$ $mol^{-1}$), the corresponding number of VEGF molecules is calculated to be approximately 9,459. This quantitative assessment highlights the presence of a detectable number of target molecules at the sensing interface, underscoring the biosensor's high sensitivity and its capability to detect analytes at ultra-low concentrations.

The EIS Nyquist plots for the non-PEG-modified biosensor, shown in Fig. 6c, reveal markedly different behaviour. Without PEG, the gold nanostructures on the electrode surface grow irregularly, leading to a less uniform morphology. As a result, the $R_{ct}$ values for the same VEGF concentrations are consistently higher, indicating reduced electron transfer efficiency. The fitted EIS parameters in Table S4 (in Supplementary Information) further illustrate the inferior electrochemical performance of the non-PEG-modified immunosensor compared to its PEG-modified counterpart. The $R_{ct}$ values remain substantially higher across all VEGF concentrations, increasing from 363 Ω at the blocking stage to 737 Ω at $10^{-10}$ g/mL, indicating limited electron transfer due to the irregular and less conductive nanostructured surface. The results are consistent with the Nyquist plots in Figure 6c, confirming that the absence of PEG leads to uncontrolled gold growth, higher interfacial resistance, and reduced sensing efficiency.

The calibration curve for the biosensor fabricated without PEG in Fig. 6d shows a limited linear dynamic range and poor sensitivity compared to the PEG-mediated sensor. The linear regression coefficient ($R^2$) drops to approximately 0.70, reflecting reduced consistency and reliability in the sensor's linear response to VEGF concentrations. Additionally, the lack of PEG results in rapid signal saturation at higher VEGF concentrations and diminished sensitivity at lower levels, further compromising the sensor's performance.

The superior linearity of the PEG-functionalized Au-based immunosensor compared to the non-PEG one originates from the decisive role of PEG in regulating gold nucleation, growth, and interfacial properties during electrodeposition. PEG modulates the formation of Au nanostructures, leading to a more uniform particle size distribution and a high–surface-area nanoarchitecture with evenly distributed active sites. This homogeneous morphology enables consistent antibody immobilization and a proportional electrochemical response to antigen concentration. In addition, PEG adsorption stabilizes the electrode interface by modulating interfacial energy, enhancing charge transfer, and reducing background noise. The resulting nanostructure exhibits increased electroactive surface area and lower charge-transfer resistance, which improve sensitivity and preserve the proportionality between antigen binding and $\Delta R_{ct}$ variation. Moreover, the PEG-mediated morphology minimizes steric hindrance and facilitates uniform diffusion of VEGF molecules, preventing localized crowding and diffusion-limited regions. Consequently, the PEG-modified electrode maintains linear

behaviour over a broader concentration range, attributed to synergistic improvements in surface homogeneity, electron transfer, and mass transport.

The data presented in Fig. 6clearly establish PEG's critical role in biosensor fabrication. By mediating the growth of gold nanostructures, PEG ensures controlled morphology, increased surface area, and enhanced electron transfer kinetics. These improvements lead to significantly better sensitivity, a broader dynamic range, and consistent signal output. The PEG-modified biosensor demonstrates a linear response across five orders of magnitude in VEGF concentrations and achieves ultra-low LODs, making it ideal for detecting biomarkers at clinically relevant levels. In contrast, the non-PEG-modified sensor suffers from poor sensitivity, limited linearity, and reduced reliability.

### 3.4. Reproducibility, Stability, and Selectivity of the Immunosensor

An experiment was performed to estimate the reproducibility of the immunosensor where the peak current response was analysed across electrodes fabricated under similar conditions. The reproducibility of the VEGF immunosensor was evaluated by fabricating four identical sensors under identical conditions and measuring their CV peak currents at a fixed VEGF concentration (Fig. 7a). The results showed negligible variation in peak currents among the sensors, with a relative standard deviation (RSD) of less than 1%. This low RSD value highlights the high reproducibility of the immunosensor, indicating that the fabrication process is consistent and reliable, thereby ensuring uniform performance across different sensors.



The stability of the immunosensor was evaluated over a four-week period using four identically fabricated sensors, each stored under identical ambient laboratory conditions and protected from air exposure. At each weekly interval, a separate sensor was tested to record its CV response. As illustrated in Fig. 7b, the peak current exhibited minimal change (less than 2%) during the observation period of 4 weeks, demonstrating the immunosensor’s ability to maintain its functionality and sensitivity over time. This remarkable stability underscores the durability of the nano-porous gold electrode and the robustness of the biofunctionalization layers, confirming the sensor's suitability for long-term applications.

The selectivity of the immunosensor was examined by exposing it to various potential interfering substances (Fig. 7c), including interleukin-1 beta (IL-1β), insulin-like growth factor 1(IGF-1), and interleukin-2 (IL-2), all at the same concentration as VEGF (1 pg/mL). The CV peak currents generated by these

interfering substances were significantly lower, amounting to less than 24% of the VEGF signal. This minimal cross-reactivity highlights the high selectivity of the immunosensor, which can be attributed to the specific binding interaction between VEGF and the immobilized surface-displayed single domain antibody on the sensor surface, as well as the effective blocking of non-specific binding sites using gelatin.

Overall, the results presented in Fig. 7 collectively demonstrate the robust performance of the fabricated VEGF immunosensor in terms of reproducibility, stability, and selectivity. The high reproducibility ensures consistent results across multiple sensors, while the stability over an extended period emphasizes the sensor's potential for long-term use. Furthermore, the exceptional selectivity against interfering biomolecules confirms its specificity for VEGF detection, establishing it as a reliable and practical tool for diagnostic applications in complex biological environments.

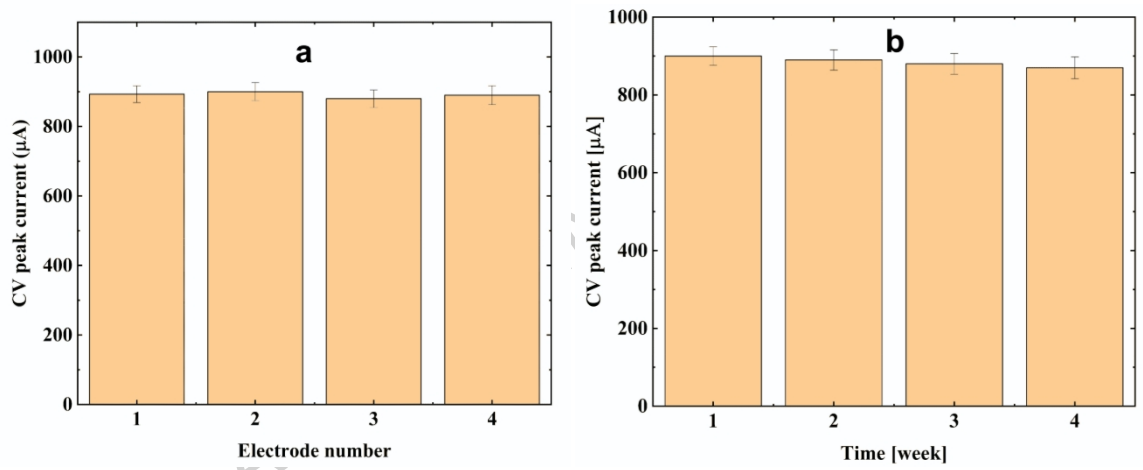

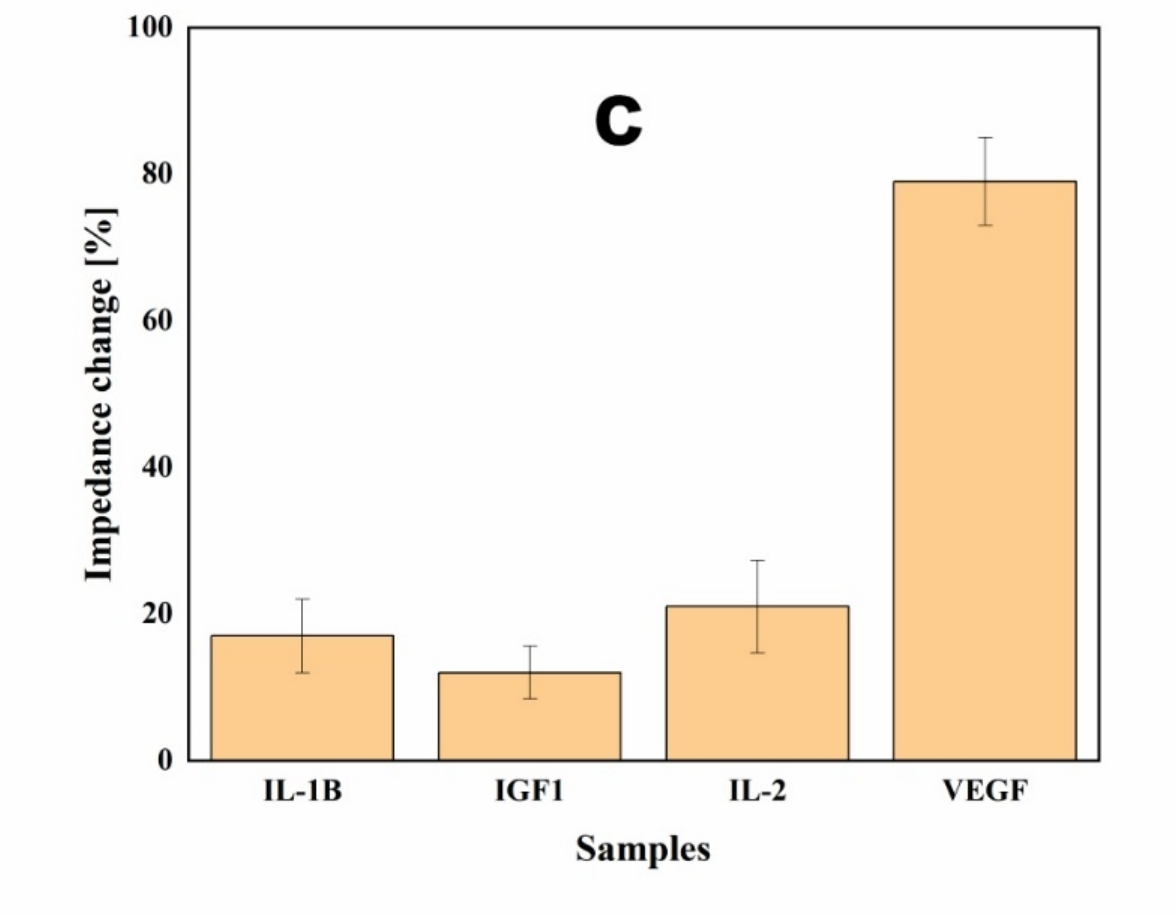


**Figure 7.** Evaluation of immunosensor performance: (a) Reproducibility based on CV measurements of four independently fabricated sensors; (b) stability test over four weeks; (c) selectivity assessment in the presence of IL-1β, IGF-1, and IL-2 (1 pg/mL each). All measurements were conducted in 0.1 M PBS (pH 7.4) containing 5 mM $[Fe(CN)_6]^{3-/4-}$ and 0.1 M KCl.

Table 1 presents a comparative evaluation of various VEGF immunosensors reported in the literature alongside the biosensor developed in this study. The proposed sensor, based on a PEG-mediated nanoporous gold electrode, demonstrates superior analytical performance, achieving an ultralow limit of detection (6 fg/mL) and a broad linear range (10 to $10^5$ fg/mL). This rare combination of high sensitivity and wide dynamic range reflects the synergistic contribution of the sensor's components. The nanoporous gold substrate enhances electron transfer and offers a high surface area for biomolecule immobilization, while VHH fragments provide strong binding affinity and stability, and gelatin contributes to biocompatibility and structural integrity. These features collectively enable highly sensitive and reliable VEGF detection, underscoring the biosensor's strong potential for biomedical applications.

**Table 1.** Comparison of the analytical capabilities of various VEGF immunosensors documented in the literature with the current research.

| Biosensor substrate | Detectionmethod | Linear range | LOD | Refs |
|---|---|---|---|---|
| Au nano-Porous/MAA/EDC NHS/VHH/Gelatin/VEGF | CV EIS | $10^{-4}$ – $10^{2}$ ng/mL | 0.5 pg/mL | [32] |
| Au/NHS/Aptamer/VEGF protein | Impedance spectra | 0.2-2 ng/mL | 200 pg/mL | [52] |
| Cellulose paper | Fluorescence control (FApt) | 100-5000 ng/mL | 137 ng/mL | [53] |
| GCE/GNRs-AuNPs/VEGF/Ab-AuNPs@PoPD | CV EIS | 0.500-500 ng/mL | 300 pg/mL | [54] |
| PEDOT-AuNP Composite material | EIS | 1-20 pg/mL | 0.5 pg/mL | [55] |
| SPE/PANI/CNT/APT | DPV | 0.5-10*$10^{6}$ pg/mL | 0.4 pg/mL | [56] |
| ITO-PET electrode | EIS | 0.1-100 pg/mL | 0.5 pg/mL | [57] |
| GCE/GNRs-AuNPs/VEGF | CV EIS | 0.5-500 ng/mL | 300 pg/mL | [58] |
| Au nano-Porous/MAA/EDC NHS/VHH/Gelatin/VEGF | CV EIS | 10 -$10^{5}$ fg/mL | 6 fg/mL | This work |
| GO/MB AuNPs | CV SWV | 2-500 pg/mL | 0.1 pg/mL | [59] |



To rigorously evaluate the analytical performance and biological applicability of the proposed immunosensor for VEGF detection, recovery experiments were conducted in both PBS and human blood serum samples at three representative concentration levels: 10 fg/mL, 1pg/mL, and 100 pg/mL. The EIS method was employed to monitor changes in charge transfer resistance ($\Delta R_{ct}$) as a function of VEGF concentration. As detailed in Table 2, the

immunosensor exhibited high recovery rates of 94.8%, 95%, and 96%, for the respective concentrations, with minimal deviation between actual and observed values. The corresponding $\Delta R_{ct}$ values demonstrated a clear and consistent concentration-dependent response, affirming the sensitivity and robustness of the detection platform. Importantly, the sensor's comparable performance in both PBS and human serum matrices indicates strong resistance to matrix effects and confirms its operational stability in complex biological fluids. These results collectively validate the immunosensor's quantitative precision, reproducibility, and suitability for accurate VEGF detection in physiologically relevant environments, underscoring its potential for future clinical and biomedical diagnostic applications.

**Table 2.** Recovery analysis of the proposed VEGF immunosensor in PBS and human serum samples at three concentrations, measured using EIS. Reported values include actual and observed concentrations, $\Delta R_{ct}$ responses, and recovery percentages, confirming the sensor's accuracy in both buffer and biological matrices.

| | In PBS | | In serum | | |
|---|---|---|---|---|---|
| Samples | Actual concentration | Actual $\Delta R_{ct}$ | Observed concentration | Observed $\Delta R_{ct}$ | Recovery |
| 1 | 10 fg/mL | 17.6 | 9.48 fg/mL | 16.7 | 94.8% |
| 2 | 1 pg/mL | 54.1 | 0.95 pg/mL | 51.4 | 95% |
| 3 | 100 pg/mL | 104.7 | 0.96 pg/mL | 100.5 | 96% |



Significantly, nonspecific biomolecules (Fig. 7c) induced only a ~20% increase in impedance, whereas VEGF produced an ~80% response. This fourfold contrast ensures that the analyte-specific $\Delta R_{ct}$ dominates the overall signal. The dendritic electrode structure, combined with uniform VHH immobilization and an effective gelatin blocking layer, restricts nonspecific adsorption to a low and reproducible level. Importantly, recovery tests in human serum (94–96%) confirm that this background variation does not compromise quantitative detection in complex biological matrices.

It is worth noting that circulating VEGF concentrations reported in human studies vary substantially depending on sample type and handling, with serum levels typically exceeding plasma values due to VEGF release from platelets during clotting [60]. Meta-analytic and clinical data indicate that VEGF concentrations in peripheral blood generally fall within the tens to hundreds of pg/mL ranges (meta-analytic mean in healthy adults ≈ 55.7

pg/mL) [61], while cancer cohorts frequently exhibit elevated serum levels reaching the high-pg to ng/mL range [62][63]. Given that our assay's detection limit (6 fg/mL, corresponding to ~9.5 × $10^3$ molecules in a 60 µL sample) lies well below typical circulating concentrations, it offers several practical advantages for diagnostics: samples can be diluted to minimize matrix effects while remaining detectable; low-volume or non-blood biological fluids (e.g., tears, bronchial washings, cerebrospinal fluid) can be analysed; and enriched subpopulations (e.g., extracellular vesicles) with low absolute VEGF content can be reliably quantified. Thus, the ultrasensitive detection limit extends the assay's applicability without exceeding clinically relevant concentration ranges.

Compared to conventional VEGF detection methods, the proposed immunosensor exhibits markedly superior sensitivity and operational simplicity. The enzyme-linked immunosorbent assay (ELISA) achieves an LOD of ~9 pg/mL[64], requires ~4.5 h, and depends on labeled antibodies. Surface plasmon resonance (SPR) achieves an LOD of ~1 pg/mL [65], but necessitates costly instrumentation and complex sample preparation. Fluorescence-based assays typically yield an LOD of ~20 pg/mL[66]and involve multi-step protocols with fluorescence readers. Chemiluminescence assays achieve an LOD of ~9 pg/mL[67], but require specialized reagents and longer assay times (~3 h). In contrast, the proposed sensor delivers a 6 fg/mL LOD with label-free detection, combining high sensitivity, low cost, and operational simplicity.



## 4. Conclusion

This study presents the development of an ultrasensitive electrochemical immunosensor for detecting VEGF, a key biomarker in cancer diagnostics. By employing a dual-phase fabrication process, i.e. integrating physical vapor deposition plus annealing, and PEG-mediated electrochemical deposition, the sensor achieved an optimized nano-porous gold electrode with enhanced surface area, conductivity, and electron transfer kinetics. PEG-mediated electrochemical modification enhances sensor performance by directing gold nanostructure growth into irregular short nanorods and small leaf-like dendrites. The biofunctionalization of the electrode with a VEGF-specific VHH antibody ensured high specificity and selectivity for VEGF detection.

Extensive characterization demonstrated the immunosensor's outstanding performance. The sensor achieved a remarkably low detection limit of 6fg/mL, with a wide dynamic range spanning several orders of magnitude.

Reproducibility tests confirmed consistent performance across fabricated sensors, while stability evaluations showed minimal signal degradation over four weeks. Selectivity experiments validated the immunosensor's ability to differentiate VEGF from potential interfering substances, ensuring reliability in complex biological samples. Notably, the PEG-directed gold morphology outperformed the non-PEG porous gold structure reported by Yarjoo et al. (LOD: 0.5 pg/mL) [28], offering approximately 100-fold higher sensitivity through optimized dendritic growth. Furthermore, this design advances the VHH-based sensing strategy introduced by Rezaei et al. [29], by integrating it with PEG-assisted gold nanostructures, enabling femtogram-level VEGF detection.

The innovative integration of nano-porous gold structures and precise biofunctionalization enabled a highly sensitive and robust platform for VEGF detection. This sensor has significant potential for early-stage cancer diagnostics, where detecting low concentrations of biomarkers is critical. Moreover, the scalable fabrication approach and long-term stability of the sensor make it a practical candidate for clinical applications and future development in biosensing technologies.



**Acknowledgements**
This work has been supported by the research council of TarbiatModares University (TMU).

**Funding declaration**
This work received institutional support from Tarbiat Modares University as part of its normal doctoral dissertation funding program. No specific grants or financial awards were provided by external public, commercial, or non-profit funding agencies for this research.

**Availability of data and materials**
The datasets used and/or analysed during the current study available from the corresponding author on reasonable request.

**Competing interests**
The authors declare no competing interests.

**References**

[1] C. I. L. Justino, A. C. Freitas, R. Pereira, A. C. Duarte, and T. A. P. Rocha Santos, ‘Recent developments in recognition elements for

chemical sensors and biosensors', *TrAC - Trends in Analytical Chemistry*, vol. 68, pp. 2–17, 2015, doi: 10.1016/j.trac.2015.03.006.

[2] A. V. Police Patil, Y. S. Chuang, C. Li, and C. C. Wu, 'Recent Advances in Electrochemical Immunosensors with Nanomaterial Assistance for Signal Amplification', *Biosensors (Basel)*, vol. 13, no. 1, 2023, doi: 10.3390/bios13010125.

[3] Y. Zheng, J. Li, B. Zhou, H. Ian, and H. Shao, 'Advanced sensitivity amplification strategies for voltammetric immunosensors of tumor marker: State of the art', *Biosens Bioelectron*, vol. 178, no. October 2020, p. 113021, 2021, doi: 10.1016/j.bios.2021.113021.

[4] K. M. Koo, N. Soda, and M. J. A. Shiddiky, 'Magnetic nanomaterial–based electrochemical biosensors for the detection of diverse circulating cancer biomarkers', *Curr Opin Electrochem*, vol. 25, p. 100645, 2021, doi: 10.1016/j.coelec.2020.100645.

[5] K. Nemčeková and J. Labuda, 'Advanced materials-integrated electrochemical sensors as promising medical diagnostics tools: A review', *Materials Science and Engineering C*, vol. 120, p. 111751, 2021, doi: 10.1016/j.msec.2020.111751.

[6] P. Skládal, 'Advances in electrochemical immunosensors for pathogens', *Curr Opin Electrochem*, vol. 14, pp. 66–70, 2019, doi: 10.1016/j.coelec.2018.12.010.

[7] L. C. Brazaca *et al.*, 'Biosensing strategies for the electrochemical detection of viruses and viral diseases – A review', *Anal Chim Acta*, vol. 1159, 2021, doi: 10.1016/j.aca.2021.338384.

[8] G. Hanrahan, D. G. Patil, and J. Wang, 'Electrochemical sensors for environmental monitoring: Design, development and applications', *Journal of Environmental Monitoring*, vol. 6, no. 8, pp. 657–664, 2004, doi: 10.1039/b403975k.

[9] H. Li, X. Hu, J. Zhao, K. Koh, and H. Chen, 'A label-free impedimetric sensor for the detection of an amphetamine-type derivative based on cucurbit[7]uril-mediated three-dimensional AuNPs', *Electrochem commun*, vol. 100, no. January, pp. 126–133, 2019, doi: 10.1016/j.elecom.2019.02.002.

[10] L. Lan, Y. Yao, J. Ping, and Y. Ying, 'Recent advances in nanomaterial-based biosensors for antibiotics detection', *Biosens Bioelectron*, vol. 91, pp. 504–514, 2017, doi: 10.1016/j.bios.2017.01.007.

[11] O. Simoska and K. J. Stevenson, ‘Electrochemical sensors for rapid diagnosis of pathogens in real time’, *Analyst*, vol. 144, no. 22, pp. 6461–6478, 2019, doi: 10.1039/c9an01747j.

[12] D. J. Hicklin and L. M. Ellis, ‘Role of the vascular endothelial growth factor pathway in tumor growth and angiogenesis’, *Journal of Clinical Oncology*, vol. 23, no. 5, pp. 1011–1027, 2005, doi: 10.1200/JCO.2005.06.081.

[13] G. Chang, H. Shu, K. Ji, M. Oyama, X. Liu, and Y. He, ‘Gold nanoparticles directly modified glassy carbon electrode for non-enzymatic detection of glucose’, *Appl Surf Sci*, vol. 288, pp. 524–529, 2014, doi: 10.1016/j.apsusc.2013.10.064.

[14] H. Shu, L. Cao, G. Chang, H. He, Y. Zhang, and Y. He, ‘Direct electrodeposition of gold nanostructures onto glassy carbon electrodes for non-enzymatic detection of glucose’, *Electrochim Acta*, vol. 132, pp. 524–532, 2014, doi: 10.1016/j.electacta.2014.04.031.

[15] Q. Zhai *et al.*, ‘Vertical Gold Nanowires Stretchable Electrochemical Electrodes’, *Anal Chem*, vol. 90, no. 22, pp. 13498–13505, 2018, doi: 10.1021/acs.analchem.8b03423.

[16] J. Zhang, M. Kambayashi, and M. Oyama, ‘A novel electrode surface fabricated by directly attaching gold nanospheres and nanorods onto indium tin oxide substrate with a seed mediated growth process’, *Electrochem commun*, vol. 6, no. 7, pp. 683–688, 2004, doi: 10.1016/j.elecom.2004.05.006.

[17] A. A. Umar and M. Oyama, ‘Growth of high-density gold nanoparticles on an indium tin oxide surface prepared using a “touch” seed-mediated growth technique’, *Cryst Growth Des*, vol. 5, no. 2, pp. 599–607, 2005, doi: 10.1021/cg049711p.

[18] V. G. Praig, G. Piret, M. Manesse, X. Castel, R. Boukherroub, and S. Szunerits, ‘Seed-mediated electrochemical growth of gold nanostructures on indium tin oxide thin films’, *Electrochim Acta*, vol. 53, no. 27, pp. 7838–7844, 2008, doi: 10.1016/j.electacta.2008.05.069.

[19] L. Suresh, P. K. Brahman, K. R. Reddy, and J. S. Bondili, ‘Development of an electrochemical immunosensor based on gold nanoparticles incorporated chitosan biopolymer nanocomposite film for the detection of prostate cancer using PSA as biomarker’, *Enzyme Microb Technol*, vol. 112, pp. 43–51, 2018, doi: 10.1016/j.enzmictec.2017.10.009.

[20] M. Khalilipour, A. Moshaii, and H. Siampour, ‘Controlled electrochemical fabrication of large and stable gold nanorods with reduced cytotoxicity’, *Sci Rep*, vol. 15, no. 1, pp. 1–14, 2025, doi: 10.1038/s41598-025-92926-5.

[21] G. Dutta, S. Nagarajan, L. J. Lapidus, and P. B. Lillehoj, ‘Enzyme-free electrochemical immunosensor based on methylene blue and the electro-oxidation of hydrazine on Pt nanoparticles’, *Biosens Bioelectron*, vol. 92, no. October, pp. 372–377, 2017, doi: 10.1016/j.bios.2016.10.094.

[22] G. Dutta and P. B. Lillehoj, ‘An ultrasensitive enzyme-free electrochemical immunosensor based on redox cycling amplification using methylene blue’, *Analyst*, vol. 142, no. 18, pp. 3492–3499, 2017, doi: 10.1039/c7an00789b.

[23] G. Dutta, D. Moschou, and R. Mandal, ‘Redox Cycling Technologies for Point-of-Care Immunodiagnostics in Various Matrices’, in *Immunodiagnostic Technologies from Laboratory to Point-Of-Care Testing*, P. Suman and P. Chandra, Eds., Singapore: Springer Singapore, 2021, pp. 75–91. doi: 10.1007/978-981-15-5823-8_4.

[24] D. Sadighbayan, M. Hasanzadeh, and E. Ghafar-Zadeh, ‘Biosensing based on field-effect transistors (FET): Recent progress and challenges’, Dec. 01, 2020, *Elsevier B.V.* doi: 10.1016/j.trac.2020.116067.

[25] S. A. Lim and M. U. Ahmed, ‘Electrochemical immunosensors and their recent nanomaterial-based signal amplification strategies: A review’, *RSC Adv*, vol. 6, no. 30, pp. 24995–25014, 2016, doi: 10.1039/c6ra00333h.

[26] Á. I. López-Lorente, ‘Recent developments on gold nanostructures for surface enhanced Raman spectroscopy: Particle shape, substrates and analytical applications. A review’, *Anal Chim Acta*, vol. 1168, 2021, doi: 10.1016/j.aca.2021.338474.

[27] S. Su *et al.*, ‘On-Electrode Synthesis of Shape-Controlled Hierarchical Flower-Like Gold Nanostructures for Efficient Interfacial DNA Assembly and Sensitive Electrochemical Sensing of MicroRNA’, *Small*, vol. 12, no. 28, pp. 3794–3801, 2016, doi: 10.1002/smll.201601066.

[28] S. Yarjoo, H. Siampour, M. Khalilipour, R. H. Sajedi, H. Bagheri, and A. Moshaii, ‘Gold nanostructure-enhanced immunosensing: ultra-sensitive detection of VEGF tumor marker for early disease diagnosis’, *Sci Rep*, vol. 14, no. 1, pp. 1–11, 2024, doi: 10.1038/s41598-024-60447-2.

[29] S. Rezaei, Z. Takalloo, Z. S. Rezaei, V. Babaeipour, A. F. Talebi, and R. H. Sajedi, ‘Soluble overexpression, high-level production and purification of receptor binding domain of human VEGF8-109 in E. coli’, *Process Biochemistry*, vol. 96, no. May, pp. 228–238, 2020, doi: 10.1016/j.procbio.2020.06.009.

[30] M. Rahmanipour, H. Siampour, A. R. Amirsoleimani, M. Rezazadeh, and A. Moshaii, ‘Cu-Ag bimetallic nanostructures with high glucose sensing performance fabricated by a scalable and reproducible method’, *Microchemical Journal*, vol. 193, no. May, p. 109208, 2023, doi: 10.1016/j.microc.2023.109208.

[31] H. Siampour, S. Abbasian, A. Moshaii, and A. R. Amirsoleimani, ‘Stable, reproducible, and binder-free gold/copper core–shell nanostructures for high-sensitive non-enzymatic glucose detection’, *Sci Rep*, vol. 12, no. 1, pp. 1–11, 2022, doi: 10.1038/s41598-022-23504-2.

[32] S. Yarjoo, H. Siampour, M. Khalilipour, R. H. Sajedi, H. Bagheri, and A. Moshaii, ‘Gold nanostructure-enhanced immunosensing: ultra-sensitive detection of VEGF tumor marker for early disease diagnosis’, *Sci Rep*, vol. 14, no. 1, pp. 1–11, 2024, doi: 10.1038/s41598-024-60447-2.

[33] Z. S. Rezaei *et al.*, ‘Differential pulse voltammetric immunosensor for direct and label-free detection of VEGF using variable domain of heavy-chain antibody displaying phage’, *Microchemical Journal*, vol. 197, no. November 2023, p. 109721, 2024, doi: 10.1016/j.microc.2023.109721.

[34] S. Alhafyan, J. Mohammadzadeh, S. S. Shahangian, and R. H. Sajedi, ‘Shining a light on VEGF detection: Phage display-mediated immuno-fluorescence assay for precise cancer biomarker analysis’, *Microchemical Journal*, vol. 212, no. January, 2025, doi: 10.1016/j.microc.2025.113053.

[35] Z. S. Rezaei *et al.*, ‘Differential pulse voltammetric immunosensor for direct and label-free detection of VEGF using variable domain of heavy-chain antibody displaying phage’, *Microchemical Journal*, vol. 197, no. November 2023, p. 109721, 2024, doi: 10.1016/j.microc.2023.109721.

[36] S. Alhafyan, J. Mohammadzadeh, S. S. Shahangian, and R. H. Sajedi, ‘Shining a light on VEGF detection: Phage display-mediated immuno-fluorescence assay for precise cancer biomarker analysis’, *Microchemical Journal*, vol. 212, no. January, 2025, doi: 10.1016/j.microc.2025.113053.

[37] M. Pak, A. Moshaii, H. Siampour, S. Abbasian, and M. Nikkhah, ‘Cobalt-copper bimetallic nanostructures prepared by glancing angle deposition for non-enzymatic voltammetric determination of glucose’, *Microchimica Acta*, vol. 187, no. 5, 2020, doi: 10.1007/s00604-020-04246-2.

[38] A. R. Amirsoleimani, H. Siampour, S. Abbasian, G. B. Rad, A. Moshaii, and Z. Zaradshan, ‘Copper oxide nanocolumns for high-sensitive non-enzymatic glucose sensing’, *Sens Biosensing Res*, vol. 42, no. September, p. 100589, 2023, doi: 10.1016/j.sbsr.2023.100589.

[39] M. Amirabadizadeh, H. Siampour, S. Abbasian, M. Nikkhah, and A. Moshaii, ‘Aptasensor for ovarian cancer biomarker detection using nanostructured gold electrodes’, *Microchimica Acta*, vol. 191, no. 1, pp. 1–11, 2024, doi: 10.1007/s00604-023-06072-8.

[40] H. Siampour, S. Abbasian, A. Moshaii, K. Omidfar, M. Sedghi, and H. Naderi-Manesh, ‘Seed-mediated Electrochemically Developed Au Nanostructures with Boosted Sensing Properties: An Implication for Non-enzymatic Glucose Detection’, *Sci Rep*, vol. 10, no. 1, pp. 1–11, 2020, doi: 10.1038/s41598-020-64082-5.

[41] S. Yarjoo, H. Siampour, M. Khalilipour, R. H. Sajedi, H. Bagheri, and A. Moshaii, ‘Gold nanostructure-enhanced immunosensing: ultra-sensitive detection of VEGF tumor marker for early disease diagnosis’, *Sci Rep*, vol. 14, no. 1, Dec. 2024, doi: 10.1038/s41598-024-60447-2.

[42] T. A. Walmsley, M. H. Abernethy, and H. P. Fitzgerald, ‘Effect of daylight on the reaction of thiols with Ellman’s reagent, 5,5’-dithiobis(2-nitrobenzoic acid)’, *Clin Chem*, vol. 33, no. 10, pp. 1928–1931, 1987, doi: 10.1093/clinchem/33.10.1928.

[43] S. R. Torati, K. C. S. B. Kasturi, B. Lim, and C. G. Kim, ‘Hierarchical gold nanostructures modified electrode for electrochemical detection of cancer antigen CA125’, *Sens Actuators B Chem*, vol. 243, pp. 64–71, 2017, doi: 10.1016/j.snb.2016.11.127.

[44] S. Rezaei, Z. Takalloo, Z. S. Rezaei, V. Babaeipour, A. F. Talebi, and R. H. Sajedi, ‘Soluble overexpression, high-level production and purification of receptor binding domain of human VEGF8-109 in E. coli’, *Process Biochemistry*, vol. 96, no. May, pp. 228–238, 2020, doi: 10.1016/j.procbio.2020.06.009.

[45] A. Bakhmachuk *et al.*, ‘Surface Plasmon Resonance Investigations of Bioselective Element Based on the Recombinant Protein A for

Immunoglobulin Detection', *Nanoscale Res Lett*, vol. 12, no. 1, Dec. 2017, doi: 10.1186/s11671-017-1903-5.

[46] M. Khalilipour, A. Moshaii, H. Siampour, S. Yarjoo, R. H. Sajedi, and J. Mohammadzadeh, 'Nanostructured gold platforms for attogram-precision cardiolipin quantification', *J Mater Chem B*, vol. 13, no. 36, pp. 11329–11341, Sep. 2025, doi: 10.1039/d5tb00798d.

[47] M. Khalilipour, A. Moshaii, and H. Siampour, 'Controlled electrochemical fabrication of large and stable gold nanorods with reduced cytotoxicity', *Sci Rep*, vol. 15, no. 1, pp. 1–14, 2025, doi: 10.1038/s41598-025-92926-5.

[48] G. Leftheriotis, S. Papaefthimiou, and P. Yianoulis, 'Dependence of the estimated diffusion coefficient of LixWO3 films on the scan rate of cyclic voltammetry experiments', *Solid State Ion*, vol. 178, no. 3–4, pp. 259–263, 2007, doi: 10.1016/j.ssi.2006.12.019.

[49] S. P. Mundinamani and M. K. Rabinal, 'Cyclic Voltammetric Studies on the Role of Electrode, Electrode Surface Modification and Electrolyte Solution of an Electrochemical Cell', *IOSR Journal of Applied Chemistry*, vol. 7, no. 9, pp. 45–52, 2014, doi: 10.9790/5736-07924552.

[50] M. Sajadpour, S. Abbasian, H. Siampour, H. Bagheri, and A. Moshaii, 'Label-free PSA electrochemical determination by seed-mediated electrochemically-deposited gold nanoparticles on an FTO electrode', *Journal of Solid State Electrochemistry*, vol. 26, no. 1, pp. 149–161, 2022, doi: 10.1007/s10008-021-05081-y.

[51] H. Siampour, S. Abbasian, A. Moshaii, K. Omidfar, M. Sedghi, and H. Naderi-Manesh, 'Seed-mediated Electrochemically Developed Au Nanostructures with Boosted Sensing Properties: An Implication for Non-enzymatic Glucose Detection', *Sci Rep*, vol. 10, no. 1, pp. 1–11, 2020, doi: 10.1038/s41598-020-64082-5.

[52] Y. Der Lin, S. I. Zida, C. C. Yang, and Y. L. Khung, 'VEGF Detection via Impedance Spectroscopy on Surface Functionalized Interdigitated Biosensor', *J Funct Biomater*, vol. 14, no. 7, Jul. 2023, doi: 10.3390/jfb14070365.

[53] E. Azuaje-Hualde, M. M. de Pancorbo, F. Benito-Lopez, and L. Basabe-Desmonts, 'Paper based microfluidic platform for single-step detection of mesenchymal stromal cells secreted VEGF', *Anal Chim Acta*, vol. 1199, p. 339588, 2022, doi: https://doi.org/10.1016/j.aca.2022.339588.

[54] M. He, P. Luo, Y. Xie, Y. He, X. Wang, and L. Tan, 'Electrochemical determination of vascular endothelial growth factor using functional

metal-polymer nanocomposites', *Colloids Surf A Physicochem Eng Asp*, vol. 677, p. 132380, 2023, doi: https://doi.org/10.1016/j.colsurfa.2023.132380.

[55] M. Kim, R. Iezzi, B. S. Shim, and D. C. Martin, 'Impedimetric biosensors for detecting vascular endothelial growth factor (VEGF) based on poly(3,4-ethylene dioxythiophene) (PEDOT)/gold nanoparticle (Au NP) composites', *Front Chem*, vol. 7, no. MAR, pp. 1–11, 2019, doi: 10.3389/fchem.2019.00234.

[56] Y. Park, M. S. Hong, W. H. Lee, J. G. Kim, and K. Kim, 'Highly sensitive electrochemical aptasensor for detecting the vegf165 tumor marker with pani/cnt nanocomposites', *Biosensors (Basel)*, vol. 11, no. 4, pp. 1–11, 2021, doi: 10.3390/bios11040114.

[57] M. Akgün and M. Kemal Sezgintürk, 'A novel biosensing system based on ITO-single use electrode for highly sensitive analysis of VEGF', *Int J Environ Anal Chem*, vol. 100, no. 4, pp. 432–450, 2020, doi: 10.1080/03067319.2019.1709637.

[58] M. He, P. Luo, Y. Xie, Y. He, X. Wang, and L. Tan, 'Electrochemical determination of vascular endothelial growth factor using functional metal-polymer nanocomposites', *Colloids Surf A Physicochem Eng Asp*, vol. 677, no. PA, p. 132380, 2023, doi: 10.1016/j.colsurfa.2023.132380.

[59] S. Ni, Z. Shen, P. Zhang, and G. Liu, 'Enhanced performance of an electrochemical aptasensor for real-time detection of vascular endothelial growth factor (VEGF) by nanofabrication and ratiometric measurement', *Anal Chim Acta*, 2020, doi: 10.1016/j.aca.2020.05.003.

[60] T. M. H. Niers, D. J. Richel, J. C. M. Meijers, and R. O. Schlingemann, 'Vascular endothelial growth factor in the circulation in cancer patients may not be a relevant biomarker', *PLoS One*, vol. 6, no. 5, 2011, doi: 10.1371/journal.pone.0019873.

[61] U. Sjöbom, A. K. Nilsson, H. Gyllensten, A. Hellström, and C. Löfqvist, 'A systematic review and meta-analysis of preanalytical factors and methodological differences influencing the measurement of circulating vascular endothelial growth factor', Jul. 01, 2022, *Public Library of Science*. doi: 10.1371/journal.pone.0270232.

[62] J. H. Guo, X. Zhu, X. T. Li, and R. J. Yang, 'Impact of serum vascular endothelial growth factor on prognosis in patients with unresectable hepatocellular carcinoma after transarterial chemoembolization',

*Chinese Journal of Cancer Research*, vol. 24, no. 1, pp. 36–43, Mar. 2012, doi: 10.1007/s11670-012-0036-8.

[63] S. Shivakumar, B. T. Prabhakar, K. Jayashree, M. G. R. Rajan, and B. P. Salimath, 'Evaluation of serum vascular endothelial growth factor (VEGF) and microvessel density (MVD) as prognostic indicators in carcinoma breast', *J Cancer Res Clin Oncol*, vol. 135, no. 4, pp. 627–636, Apr. 2009, doi: 10.1007/s00432-008-0497-9.

[64] 'Human VEGF ELISA Kit – Quantikine, https://www.rndsystems.com/products/human-vegf-quantikine-elisa-kit_dve00'.

[65] L. Oldak *et al.*, 'An Array SPRi Biosensor for Simultaneous VEGF-A and FGF-2 Determination in Biological Samples', *Applied Sciences*, vol. 12, no. 24, 2022, doi: 10.3390/app122412699.

[66] Q. Zhou *et al.*, 'Ultrasensitive enzyme-free fluorescent detection of VEGF165 based on target-triggered hybridization chain reaction amplification', *RSC Adv*, vol. 8, no. 46, pp. 25955–25960, 2018, doi: 10.1039/c8ra04721a.

[67] I. A. Darwish, N. Z. Alzoman, and N. N. Khalil, 'A Novel Highly Sensitive Chemiluminescence Enzyme Immunoassay with Signal Enhancement Using Horseradish Peroxidase-Luminol-Hydrogen Peroxide Reaction for the Quantitation of Monoclonal Antibodies Used for Cancer Immunotherapy', *Chemosensors*, vol. 11, no. 4, 2023, doi: 10.3390/chemosensors11040245.